Publication Year	2019
Acceptance in OA@INAF	2020-12-14T10:30:50Z
Title	XMM-Newton and INTEGRAL analysis of the Supergiant Fast X-ray Transient IGR J17354-3255
Authors	Goossens, M. E.; Bird, A. J.; Hill, A. B.; SGUERA, VITO; Drave, S. P.
DOI	10.1093/mnras/sty3236
Handle	http://hdl.handle.net/20.500.12386/28820
Journal	MONTHLY NOTICES OF THE ROYAL ASTRONOMICAL SOCIETY
Number	485

Monthly Notices
of the
ROYAL ASTRONOMICAL SOCIETY

MNRAS **485,** 286–298 (2019)
Advance Access publication 2018 December 6

doi:10.1093/mnras/sty3236

XMM–Newton and *INTEGRAL* analysis of the Supergiant Fast X-ray Transient IGR J17354−3255

M. E. Goossens,[1★] A. J. Bird,[1★] A. B. Hill,[1] V. Sguera[2] and S. P. Drave[1]

[1]*School of Physics and Astronomy, Faculty of Physical Sciences and Engineering, University of Southampton, SO17 1BJ, UK*
[2]*INAF-OAS, Osservatorio di Astrofisica e Scienza dello Spazio di Bologna, Area della Ricerca del CNR, via Gobetti 101, I-1-40129 Bologna, Italy*

Accepted 2018 November 20. Received 2018 November 4; in original form 2018 February 1

ABSTRACT

We present the results of combined *INTEGRAL* and *XMM–Newton* observations of the supergiant fast X-ray transient (SFXT) IGR J17354−3255. Three *XMM–Newton* observations of lengths 33.4, 32.5, and 21.9 ks were undertaken, the first an initial pointing to identify the correct source in the field of view and the latter two performed around periastron. Simultaneous *INTEGRAL* observations across ∼66 per cent of the orbital cycle were analysed but the source was neither detected by IBIS/ISGRI nor by JEM-X. The *XMM–Newton* light curves display a range of moderately bright X-ray activity but there are no particularly strong flares or outbursts in any of the three observations. We show that the spectral shape measured by *XMM–Newton* can be fitted by a consistent model throughout the observation, suggesting that the observed flux variations are driven by obscuration from a wind of varying density rather than changes in accretion mode. The simultaneous *INTEGRAL* data rule out simple extrapolation of the simple power-law model beyond the *XMM–Newton* energy range.

Key words: stars: winds, outflows – X-rays: binaries – X-rays: individual: (IGR J17354−3255).

1 INTRODUCTION

Supergiant Fast X-ray Transients (SFXTs) consist of a compact object, which is either a neutron star or black hole, orbiting a supergiant donor and accreting from its wind (Sguera et al. 2005, 2006; Negueruela et al. 2006). These sources are a subclass of high-mass X-ray binaries (HMXBs) which are occasionally observed in X-ray quiescence ($L_x < 10^{32}$ erg s^{-1}) but more frequently during a low X-ray state. Occasionally, fast X-ray transient activity can be observed from these binary systems, this being characterized by outbursts lasting less than a day and flares of a few tens of minutes and peak luminosities of $\sim 10^{36}$ erg s^{-1} similar to those of persistent supergiant X-ray binaries (SGXBs; Walter & Zurita Heras 2007).

SFXT systems are generally identified by their low persistent luminosity and their high dynamic range on variable time-scales ($\sim 10^3$–10^5 times the range observed in classical systems; Sguera et al. 2005; Romano et al. 2015). The origin of this behaviour is still a matter of debate, with several viable models used to explain this phenomenon. These models range from accretion of dense inhomogeneous 'clumps' in the winds of the supergiant companions (in 't Zand 2005; Ducci et al. 2009), to the presence of magnetic/centrifugal gates generated by the neutron stars (Bozzo, Falanga & Stella 2008), to a subsonic settling accretion regime combined with magnetic reconnections (Shakura et al. 2014).

IGR J17354−3255 was discovered in 2006 April as an unidentified hard X-ray transient during a monitoring observation of the Galactic bulge region (Kuulkers et al. 2006, 2007) with the INTErnational Gamma-Ray Astrophysics Laboratory (*INTEGRAL*). The source reached a flux of $\sim 2.1 \times 10^{-10}$ erg cm^{-2} s^{-1} (18 mCrab) in the 20–60 keV band during two consecutive 1.8 ks pointings and was located towards the Galactic Centre. IGR J17354−3255 is reported in the latest IBIS catalogue (Bird et al. 2016) as a persistent source with an average flux of 8.33×10^{-12} erg cm^{-2} s^{-1} (1.1 mCrab) in the 20–40 keV energy band.

IGR J17354−3255 is also listed in the *Swift* Burst Alert Telescope (BAT; Barthelmy et al. 2005) 58 month Hard X-ray Survey (Baumgartner et al. 2010) with a 14–195 keV average flux of 2.7×10^{-11} erg cm^{-2} s^{-1} as well as the 54 month Palermo *Swift*/BAT hard X-ray catalogue (Cusumano et al. 2010) with a 15–150 keV average flux of 2.1×10^{-11} erg cm^{-2} s^{-1}.

Due to its hard X-ray flaring activity with a mean flaring flux of 2.6–5.2 $\times$ 10^{-12} erg cm^{-2} s^{-1} (20–40 mCrab) and peak flaring flux of 1.4×10^{-9} erg cm^{-2} s^{-1} (108 mCrab) in the 18–60 keV energy band, together with its large dynamic range, Sguera et al. (2011) proposed IGR J17354−3255 as a candidate intermediate SFXT much like IGR J16465−4507 (Clark et al. 2010) and several others (Sguera et al. 2007; Walter & Zurita Heras 2007). The X-ray dynamic range was further increased by a

★ E-mail: M.E.Goossens@soton.ac.uk (MEG); A.J.Bird@soton.ac.uk (AJB)

© 2018 The Author(s)
Published by Oxford University Press on behalf of the Royal Astronomical Society

Downloaded from https://academic.oup.com/mnras/article/485/1/286/5232390 by CNR user on 14 December 2020

non-detection during observations with *XMM–Newton* (Bozzo et al. 2012), giving support for the classification of this source as an SFXT.

D'Aì et al. (2011) and Sguera et al. (2011) studied the hard X-ray properties of IGR J17354−3255 using archival *Swift*/BAT and *INTEGRAL* observations, respectively. They discovered a periodic signal of 8.447 ± 0.002 d, which they interpreted as the orbital period of the binary system.

Chandra observations (Tomsick et al. 2009) reduced the X-ray error box of the source to arcsec size consequently allowing identification of the optical/infrared counterpart. Coleiro et al. (2013) subsequently measured the nIR K_s-band spectrum for IGR J17354−3255 suggesting that the supergiant spectral type is likely an O8.5Iab(f) or an O9Iab, further confirming the sgHMXB/SFXT classification. Its high optical/IR extinction and the position within 5 degrees of the Galactic Centre may indicate a distance near 8.5 kpc (Tomsick 2009).

IGR J17354−3255 has been proposed as the best candidate counterpart of the gamma-ray transient AGL J1734−3310 based on spatial correlation as well as on a similar flaring nature on short time-scales (Sguera et al. 2011; Sguera 2013). IGR J17354−3255 is the only hard X-ray source that can be unambiguously said to be located within the 0.46 degrees error circle radius of AGL J1734−3310. The latter is an MeV transient source discovered by *AGILE*/GRID in 2009 April during a 1 d duration flare (Bulgarelli et al. 2009).

More recently, Ducci et al. (2013) performed the first full-orbital monitoring of this source with *Swift*/XRT and Bozzo et al. (2017) included IGR J17354−3255 in a comprehensive *XMM–Newton* study of several SFXTs aiming to investigate their accretion environment.

In this paper, we report on three *XMM–Newton* observations together with a simultaneous *INTEGRAL* observation of IGR J17354−3255 where the source exhibits typical SFXT behaviour with a high level of flaring activity, although no particularly bright outbursts are seen.

2 OBSERVATIONS AND DATA REDUCTION

2.1 *INTEGRAL*

The *INTEGRAL* gamma-ray observatory consists of three co-aligned coded mask telescopes: the soft X-ray monitor (JEM-X; Lund et al. 2003), the spectrometer (SPI; Vedrenne et al. 2003) and the hard X-ray imager (IBIS; Ubertini et al. 2003). *INTEGRAL* observations are usually divided into science windows that have a duration of ∼2000 s. Data from IBIS and JEM-X were analysed using the 'Off-line Scientific Analysis' (OSA) software version 10.0.

IGR J17354−3255 was in the IBIS/ISGRI fully coded field of view (FOV) (during a hexagonal dither pointing) for a total exposure of ∼145 ks during a proprietary targeted observation (PI Drave), which formed part of revolution 1277. However, by chance it was also in the FOV during the remaining part of revolution 1277 (for an additional total on-source exposure of ∼54 ks) as well as during the previous revolution 1276 (for an on-source exposure of ∼130 ks). Combining all the data from the two revolutions results in a total on-source exposure of 329 ks meaning that about 66 per cent of an entire orbital cycle of IGR J17354−3255 is covered (Fig. 1).

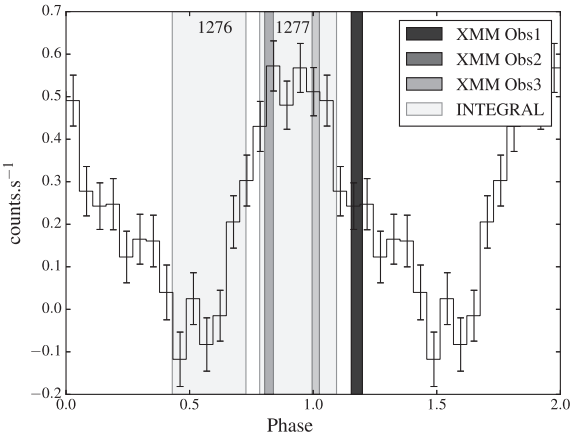

Figure 1. Phase folded light curve of the IBIS/ISGRI data set for IGR J17354−3255 in the 18–60 keV energy band with the ephemeris MJD 55925.895 as phase = 0 and a period of 8.447 d. The durations of the three *XMM–Newton* observations as well as the 327 ks on-source *INTEGRAL* coverage are indicated according to phase. The two *INTEGRAL* revolutions are marked by their respective numbers.

2.2 *XMM–Newton*

IGR J17354−3255 was observed with *XMM–Newton* in three observations between 2013 March 15 and March 31; details are given in Table 1. The *XMM–Newton Observatory* consists of three 1500 cm^2 X-ray telescopes each carrying an European Photon Imaging Camera (EPIC) at the focus. Two of the EPICs use Metal Oxide Semiconductor (MOS) CCDs (Turner et al. 2001) and one uses a pn-CCD (Strüder et al. 2001). Additionally, there are Reflection Grating Spectrometer (RGS; den Herder et al. 2001) arrays located behind two of the telescopes.

The first observation was performed as an initial pointing to identify the correct source in the FOV. As a result IGR J17354−3255 was only observed with the MOS1 and MOS2 cameras but not with the PN. This was corrected for the consecutive observations so that the source was in the centre of the FOV. To schedule these observations an ephemeris of MJD 55924.959 was used as this was the best estimate of the periastron location at the time. We have subsequently calculated a refined ephemeris MJD 55925.895 using the 12 yr of *INTEGRAL* data available for this source. This first observation was thus performed at an orbital phase range of ϕ = 0.154–0.199. Observations 2 and 3 were performed at phase ranges ϕ = 0.804–0.839 and ϕ = 0.996–0.025, respectively, so shortly before and approximately at periastron, using this refined ephemeris as phase = 0 and a period of 8.447 d (Fig. 1). In observation 1 both EPIC-MOS cameras were operated in full-frame mode and in observations 2 and 3 both EPIC-MOS cameras as well as the EPIC-pn camera were operated in large window mode. In each case medium thickness filters were used in case of intense flaring behaviour.

Observation data files (ODFs) were processed to produce calibrated event lists using the Science Analysis System (SAS) v15.0.0. RGS data was processed using the RGSPROC task but the resulting FITS files had no counts for IGR J17354−3255 so that no further analysis was carried out for these instruments. We reprocessed the EPIC-MOS and EPIC-pn events files with the EMPROC and EPPROC tasks, respectively. The data sets were checked for regions of high particle background following the method outlined in the

Downloaded from https://academic.oup.com/mnras/article/485/1/286/5232390 by CNR user on 14 December 2020

Table 1. *XMM–Newton* observation log for IGR J17354−3255. The effective exposure corresponds to the exposure assigned to the source position after filtering and cleaning processes.

Obs. No.	Date	S/C Rev.	Obs. ID	Start (UT)	Stop (UT)	Tot. Exp. (ks)	Eff. Exp. (ks)		
							EPIC-MOS1	EPIC-MOS2	EPIC-pn
1	15 Mar. 2013	2429	0693900201	13:04:56	22:21:52	33.416	33.076	33.128	0
2	29 Mar. 2013	2436	0701230101	11:48:26	20:50:44	32.538	25.101	25.116	24.082
3	31 Mar. 2013	2437	0701230701	03:35:07	08:40:24	21.917	21.630	21.635	19.685

XMM–Newton SAS data analysis threads (Gabriel et al. 2004).[1] We created single-event (PATTERN = = 0) light curves above 10 keV for EPIC-MOS1 and EPIC-MOS2 and between 10 and 12 keV for pn covering the full FOV of each instrument using cut-offs between 0.2 and 0.4 counts s^{-1} as appropriate. The good time intervals (GTIs) that remained after this filtering process were used in EVSELECT to produce filtered event files, resulting in the relevant effective exposure times reported in Table 1.

Source and background extraction regions were selected to optimize signal to noise using the EREGIONANALYSE tool, but selections were subject to limitations such as the presence of chip gaps, and the changing observation configuration between observations 1 and 2. The radius of each source region was chosen to be as wide as possible to encompass most of the source photons; the recommended value corresponds to an encircled energy fraction of ∼80 per cent from the MOS and pn cameras according to the SAS users' handbook.[2] As can be seen in Fig. 2, however, the source was sometimes located close to the edge of a CCD so that the radius had to be restricted so as to avoid the collection of photons from adjacent CCDs. In particular, the source region radius for the EPIC-pn camera in observation 3 had to be limited due to the source's extreme proximity to the chip gap.

The background regions were nominally chosen to be about twice the size as the source regions subject to sufficient available space on the CCD (Fig. 2), but that was compromised heavily in the observations where the EPIC-MOS cameras were in large window mode, where the source and background regions were eventually of similar size. Any differences in size of the source and background extraction areas were accounted for using the BACKSCALE and LCCORR SAS tasks for the spectra and light curves, respectively.

The maximum count rates of both the EPIC-MOS1 and EPIC-MOS2 cameras in observation 1 are slightly more than twice the tolerance limits for pile-up mentioned in Jethwa et al. (2015), and this observation may therefore be affected by pile-up, likely due to operation in full frame mode. This is not the case for either of the cameras in the other two observations that were performed in large window mode. For completeness, all data sets were assessed for photon pile-up, using the EPATPLOT task, which compares the observed-to-model fractions for single and double events. As expected based on the count rates, all single/double fractions were consistent with the nominal value of 1.0 within statistical errors (1σ) and there was good graphical agreement between the observed and expected pattern distributions. We conclude that observations 2 and 3 are not affected by pile-up. In both cameras for observation 1 the single/double event fractions are not always consistent with

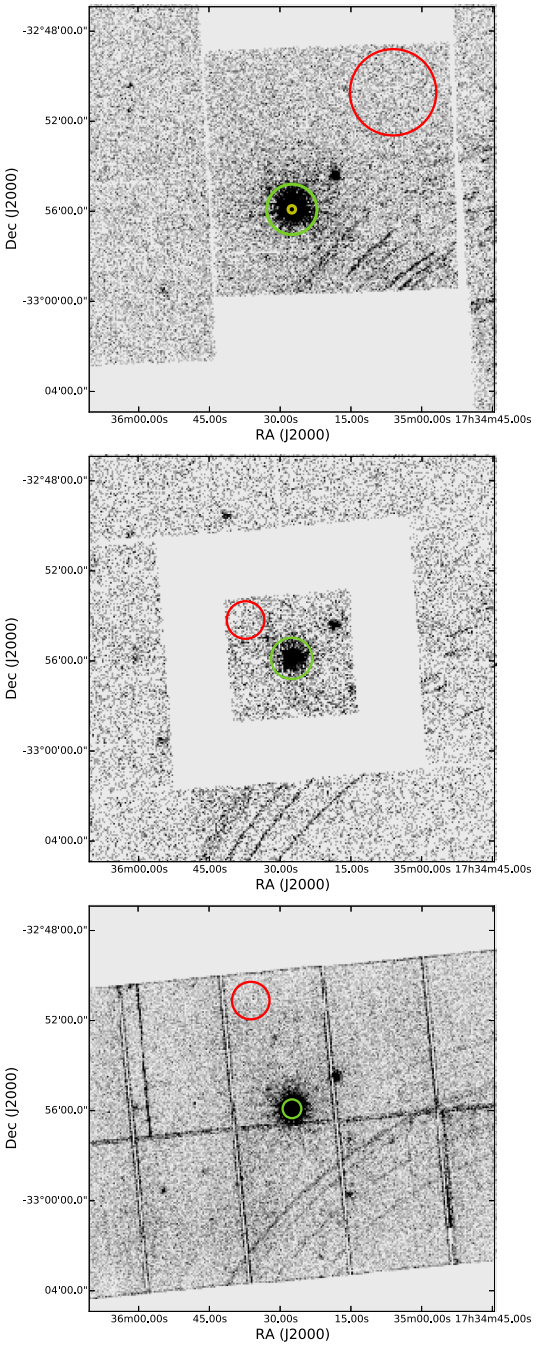

Figure 2. EPIC-MOS1, EPIC-MOS2, and EPIC-pn images for observations 1, 2, and 3, respectively. The source and background extraction regions are shown as green and red circles, respectively. The excised inner source region in observation 1 is shown in yellow.

[1] https://www.cosmos.esa.int/web/xmm-newton/sas-threads
[2] https://xmm-tools.cosmos.esa.int/external/xmm_user_support/documentation/sas_usg/USG/

Downloaded from https://academic.oup.com/mnras/article/485/1/286/5232390 by CNR user on 14 December 2020

1.0 implying that this observation may be affected by pile-up. In order to mitigate any pile-up, the core of the PSF was excised using an annular region around the centroid until the observed pattern distributions matched the expected ones and the single/double event fractions were consistent with 1.0. It was found that an annular inner radius of 200 physical pixels provided the best result for both EPIC-MOS1 and EPIC-MOS2 cameras.

The resulting coordinates for both the source and background regions can be found in Table 2.

All light curves and spectra reported in this paper were extracted following the standard procedures. The SAS tools RMFGEN and ARFGEN were used to generate the response and ancillary matrix files. The files were grouped using the SPECGROUP task with a minimum of 25 counts per bin and a maximum oversampling factor of three. Spectra were fitted with models using XSPEC version 12.8.2 where the uncertainties quoted are at the 90 per cent confidence level and the elemental abundances are set to those of Wilms, Allen & McCray (2000).

3 ANALYSIS AND RESULTS

3.1 *INTEGRAL*

3.1.1 IBIS/ISGRI

All available science windows covering the period from 2013 March 26 05:13 UTC to 2013 March 28 17:38 UTC for revolution 1276 and 2013 March 29 04:55 UTC to 2013 March 31 19:56 UTC for revolution 1277 were analysed. The source was not detected by IBIS/ISGRI in either energy bands (18–60 keV or 60–100 keV) in each single science window, in each single revolution significance map (1276, 1277), or in the summed revolution significance map 1276 + 1277. In the latter case (329 ks exposure) the 3σ upper limit on the persistent flux is 0.77 mCrab or 1×10^{-11} erg cm^{-2} s^{-1} (18–60 keV) while the 3σ upper limit from the single revolution 1277 around the periastron passage (143 ks exposure) is 1.04 mCrab or 1.35×10^{-11} erg cm^{-2} s^{-1} (18–60 keV).

3.1.2 JEM-X

We analysed all available JEM-X data acquired simultaneously with IBIS/ISGRI data during revolution 1277. IGR J17354−3255 was in the JEM-X fully coded FOV at all times, however, it was not detected in a combined mosaic of JEM-X1 and JEM-X2 (185 ks combined exposure) in either the 3–10 keV or 10–20 keV energy bands. The 3σ upper flux limit was found to be 1.35×10^{-11} erg cm^{-2} s^{-1} (0.9 mCrab) in the 3–10 keV band.

3.2 *XMM–Newton*

The background-subtracted light curves of IGR J17354−3255 are shown in Fig. 3. As previously mentioned there was no EPIC-pn data in the first observation for this source. The light curves display moderately bright X-ray flares but there are no particularly strong outbursts in any of the three observations. The flux of the two flares in observation 1, $\sim 4 \times 10^{-11}$ erg cm^{-2} s^{-1}, is significantly higher than the average flux in observations 2 and 3, $\sim$1.2–2.5 $\times 10^{-11}$ erg cm^{-2} s^{-1}. These two flares each lasted for $\sim$7 ks with a $\sim$13 ks gap between them. To date the strongest flare detected in the soft X-rays is the one detected by XRT (8.7×10^{-11} erg cm^{-2} s^{-1} (Sguera et al. 2011). The two flares detected by *XMM–Newton* have a flux that is of the same order

Table 2. Source and background regions. In each case, the co-ordinates of the centre of the region are given and the radius (or range of radii for annular regions) is specified in physical pixels.

Observation	Source Region		Background Region			
	EPIC-MOS1	EPIC-MOS2	EPIC-pn	EPIC-MOS1	EPIC-MOS2	EPIC-pn
1	(22675.2, 22446.4, 200 − 1340)	(22678.3, 22459, 200 − 1420)	–	(28060.5, 28660.5, 2300)	(27980.5, 28620.5, 2100)	–
2	(24928, 24116.5, 1020)	(24945.9, 24126.5, 1100)	(24943.8, 24112, 400)	(22310.5, 26470.5, 1000)	(22490.5, 26170.5, 1000)	(22680.5, 29640.5, 1000)
3	(24965.3, 24104.4, 1420)	(24970.5, 24103.1, 1200)	(24976.8, 24093.8, 400)	(22330.5, 26250.5, 1000)	(24340.5, 26220.5, 800)	(22780.5, 29860.5, 1000)

Downloaded from https://academic.oup.com/mnras/article/485/1/286/5232390 by CNR user on 14 December 2020

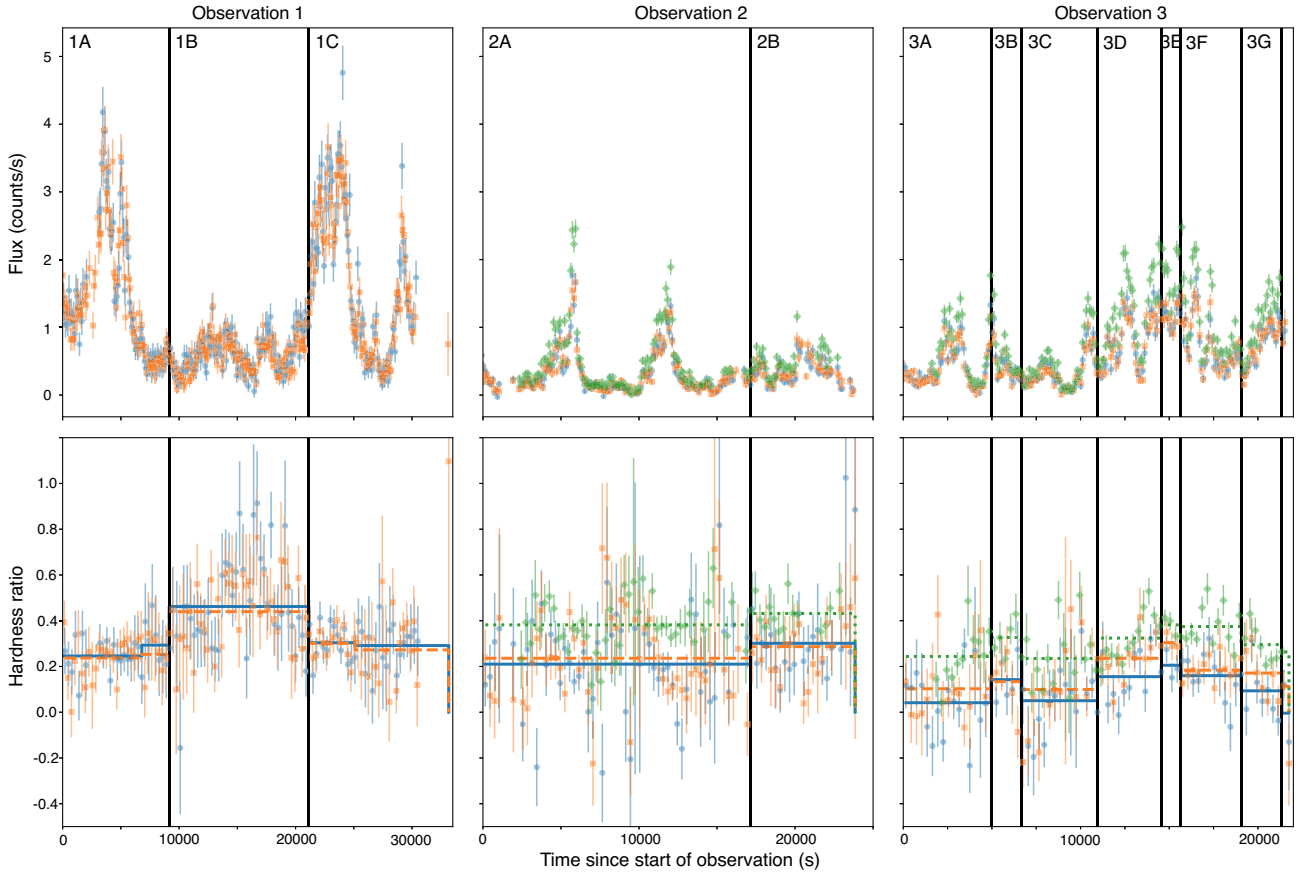

Figure 3. Top panel: Light curves of the three observations in EPIC-MOS (blue and orange) and EPIC-pn (green) cameras. EPIC-pn fluxes are scaled by a factor of 0.5. Bottom panel: Bayesian block analysis of the hardness ratios for the three observations where the different blocks suggest the optimal segmentation of the data. The vertical lines represent the time stamps at which the observations were split into different sections, annotated as 1A-3G.

of magnitude as the XRT flare. The corresponding exposure times of the different cameras are outlined in Table 1.

3.3 Spectral variability

We constructed light curves with a 300 s binning in soft (0.2–4 keV) and hard (4–10 keV) energy bands in order to investigate how the hardness ratio (HR) varies with time. This bin size was chosen (by inspection) as a compromise between having sufficient resolution to follow the rapid changes in source flux and retaining useful statistics within each bin.

$$HR = \frac{H - S}{H + S} \tag{1}$$

The HR light curve is shown in Fig. 3 (lower), and indicates that the spectral shape was changing during observation 1, likely remained the same during observation 2 and changed more variably during observation 3. To objectively characterize any changes in hardness during the three observations we used the refined Bayesian blocks method of Scargle et al. (2013) to partition the data set into sections with consistent HR. The purpose of the algorithm is to identify and characterize statistically significant variations using a simple non-parametric model that finds the optimal segmentation of the data without making any assumptions about the time-scales or amplitude/shape of variations (Hill 2016). Additionally, the algorithm can perform multivariate analysis so that the data from both the EPIC-MOS1 and EPIC-MOS2 cameras, as well as the EPIC-pn camera where available, could be modelled simultaneously (Fig. 3). The small discrepancies between blocks, detected in different cameras, are due to differences in their spectral responses.

From this analysis it is clear that the spectrum of IGR J17354−3255 hardens during a part of observation 1 extending from ∼9145–21150 s from the start of the observation. Consequently, we split the data from observation 1 into three distinct sections (labelled 1A, 1B, and 1C) where the source spectrum transitions from being soft to harder and back to softer. When the source spectrum is softer the corresponding flux is greater, and vice versa. This may indicate that a dense clump of material is present in between the flares obscuring the source from view (see Section 4 Discussion).

In the second observation, the source is in a state of low level activity. Small fluctuations can be seen in the light curve, however the Bayesian block analysis suggests only two segmentations from the hardness ratios. These are only minimally different so that we did not expect them to represent any significant spectral variations. For the sake of consistency we split the observation into two sections labelled 2A and 2B.

Inspection of the light curve for observation 3 suggests that IGR J17354−3255 was undergoing flaring activity on short time-scales. Indeed the Bayesian block analysis suggests several segmentations when considering the HR. The differences between the sections are significant enough to warrant creating separate spectra for each; hence observation 3 was split into seven sections. There were

Downloaded from https://academic.oup.com/mnras/article/485/1/286/5232390 by CNR user on 14 December 2020

Table 3. Observation subsections derived from the Bayesian blocks analysis. Start and stop times are relative to the start of each observation.

Section	Tstart [s]	Tstop [s]	Exposure [ks]
1A	0	9150.0	9.20
1B	9150.0	21150.0	12.0
1C	21150.0	33100.0	12.0
2A	0	17152.6	17.2
2B	17152.6	24100.0	7.00
3A	0	4950.0	4.95
3B	4950.0	6653.0	1.73
3C	6653.0	10950.0	4.30
3D	10950.0	14550.8	3.60
3E	14550.8	15653.0	1.10
3F	15653.0	19050.0	3.40
3G	19050.0	21353.0	2.30

insufficient counts in the final segment (from ∼21353 s after the start time of the EPIC-MOS1 camera until the end of the observation) to create valid spectra.

The observation subsections derived from the Bayesian blocks analysis and used in the subsequent spectral analysis are listed in Table 3.

3.4 Spectral analysis

Spectra were extracted for the individual sections and fitted with models using XSPEC version 12.8.2. The CFLUX model within XSPEC was used to give the unabsorbed flux of the entire model (CFLUX is a convolution model designed to determine the flux of a model or model component over a specified energy range). A constant was used during simultaneous fitting in order to account for the difference between the EPIC-MOS and EPIC-pn cameras. Currently the instruments return energy-dependent flux differences of up to 7 per cent for broad-band sources (Read, Guainazzi & Sembay 2014). Slight differences can occur between the two EPIC-MOS cameras due to different amounts of photons being received at the same time. The fit parameters resulting from all models are outlined in full in Tables 4, 5, 6, and 7.

3.4.1 Observation 1

The first observation was divided into three sections based on the Bayesian block analysis of the HR evolution (Fig. 3). For each of the sections the spectra obtained from the EPIC-MOS1 and EPIC-MOS2 cameras were fit simultaneously in the 1–12 keV energy range. A Tuebinger–Boulder ISM absoprtion model with a power law (CONST∗TBABS∗(POWERLAW)) as well as one with a blackbody (CONST∗TBABS∗(BLACKBODY)) resulted in acceptable fits (Table 4).

Inspection of the residuals for each section showed evidence of an emission feature consistent with a 6.4 keV iron-Kα line. Consequently, to further characterize the spectral shape the spectrum was fit with an absorbed power-law or blackbody continuum with an additional Gaussian component (CONST∗TBABS∗(POWERLAW + GAUSSIAN)), (CONST∗TBABS∗(BLACKBODY + GAUSSIAN)). The absorption, power-law index, temperature, Gaussian line energy, and line width were left as free parameters.

We found that the spectrum was well fit by this model in the case of an absorbed blackbody continuum (Table 7). When fitting an absorbed power law not all sections had sensible parameters (Table 6).

While the power-law indices in sections 1A and 1C are consistent within errors it is apparent that the photon index in section 1B is slightly lower in comparison confirming that the source enters a harder spectral state during this time as was suggested by the HR analysis in Section 3.1. A significant variation in hydrogen column density as part of the absorbed power-law model can also be seen with an $N_{\rm H}$ of $\sim 12 \times 10^{22}\,{\rm cm}^{-2}$ in section 1A, increasing to $\sim 17 \times 10^{22}\,{\rm cm}^{-2}$ in section 1B and finally decreasing again to $\sim 14 \times 10^{22}\,{\rm cm}^{-2}$ in section 1C. The Gaussian line energy is consistent within errors between sections with an average value of ∼6.38 keV. The Gaussian line widths correspond to an electron plasma temperature of $\sim 6 \times 10^5$ K which is well in excess of that expected for a supergiant atmosphere. This phenomenon can also be seen for some of the Gaussian line widths in the following two observations and is likely due to low signal-to-noise ratio. The EW of the line appears to be lower during the two flares compared to the gap between them suggesting that the iron emission is stronger between the two flares. The source was observed at an initial X-ray flux of $\sim 3.8 \times 10^{-11}\,{\rm erg\,cm^{-2}\,s^{-1}}$corresponding to an X-ray luminosity of 3.30×10^{35} (assuming a distance of 8.5 kpc, as derived from the closeness to the Galactic centre and the high X-ray absorption (Tomsick et al. 2009). There is a decrease in flux in section 1B and then again an increase in section 1C, coinciding with the previously mentioned differences in $N_{\rm H}$. Additionally, a small improvement in the residuals can be noted as the iron emission feature is introduced. These small improvements suggest that there likely is an iron emission feature present.

3.4.2 Observation 2

The second observation was analysed in two sections as suggested by the Bayesian block analysis. The spectra extracted from the EPIC-MOS1, EPIC-MOS2, and EPIC-pn cameras were fitted simultaneously. We used the energy range 1–12 keV for the two EPIC-MOS cameras and 1–15 keV for the EPIC-pn camera. An absorbed power-law model (CONST∗TBABS∗(POWERLAW)) resulted in acceptable fits with $\chi^2_{\rm red}$/d.o.f = 1.23/324 and $\chi^2_{\rm red}$/d.o.f = 1.16/254 (Table 4) for sections 2A and 2B, respectively. The hydrogen column density in section 2A is slightly lower than it was in the first observation whilst the one in section 2B is approximately the same as that from section 1A. The photon indices are consistent within errors with those of sections 1A and 1C, respectively. The parameters compare similarly between the sections when using an absorbed blackbody model (CONST∗TBABS∗(BLACKBODY)). The hydrogen column density is generally lower in the two sections in the second observation whilst the photon indices are consistent within errors with those of sections 1A and 1C. Considering there was evidence of a ∼6.4 keV iron-Kα line in observation 1 we inspected these spectra for the same feature. Consequently, we added a Gaussian component to the models (CONST∗TBABS∗(POWERLAW + GAUSS)), (CONST∗TBABS∗(BLACKBODY + GAUSS). Unlike the first observation, the fits did not improve as much in this one and the iron lines are at different energies and do not have constrained values for the respective equivalent widths. All fit parameters for this observation for the two different models are outlined in Tables 4–A1.

3.4.3 Observation 3

Observation 3 was divided into seven sections. For each of the sections the spectra obtained from the EPIC-MOS1, EPIC-MOS2, and EPIC-pn cameras were fitted simultaneously using the same

Downloaded from https://academic.oup.com/mnras/article/485/1/286/5232390 by CNR user on 14 December 2020

Table 4. Spectral parameters for each sub-observation obtained using a TBABS∗(POWERLAW) model. Uncertainties quoted are at the 90 per cent confidence level.

Section	N_H [$\times 10^{22}$ cm^{-2}]	Γ	Unabsorbed Flux [$\times 10^{-11}$ erg cm^{-2} s^{-1}]	Luminosity [$\times 10^{35}$ erg s^{-1}]	χ^2_{red}/d.o.f
1A	12.1 ± 0.5	1.26 ± 0.07	5.5 ± 0.2	4.77	1.42/175
1B	17 ± 1	1.0 ± 0.1	2.8 ± 0.2	2.46	1.23/132
1C	14.1 ± 0.5	1.30 ± 0.07	5.9 ± 0.2	5.06	1.43/199
2A	10.8 ± 0.3	1.27 ± 0.04	1.12 ± 0.03	0.90	1.23/324
2B	12.7 ± 0.6	1.42 ± 0.07	1.18 ± 0.06	1.02	1.16/254
3A	8.1 ± 0.4	1.47 ± 0.07	1.23 ± 0.05	1.07	1.17/206
3B	8.2 ± 0.5	1.16 ± 0.09	1.8 ± 0.1	1.53	1.59/117
3C	7.4 ± 0.4	1.19 ± 0.07	1.09 ± 0.06	0.94	1.14/178
3D	8.4 ± 0.3	1.07 ± 0.05	2.8 ± 0.1	2.43	1.32/254
3E	8.3 ± 0.2	0.97 ± 0.04	3.3 ± 0.1	2.85	1.27/298
3F	9.7 ± 0.3	1.23 ± 0.05	2.6 ± 0.1	2.27	1.38/247
3G	8.5 ± 0.4	1.34 ± 0.06	2.4 ± 0.1	2.06	1.08/199

Table 5. Spectral parameters for each sub-observation obtained using a TBABS∗(BLACKBODY) model. Uncertainties quoted are at the 90 per cent confidence level.

Section	N_H [$\times 10^{22}$ cm^{-2}]	kT [keV]	Unabsorbed Flux [$\times 10^{-11}$ erg cm^{-2} s^{-1}]	Luminosity [$\times 10^{35}$ erg s^{-1}]	χ^2_{red}/d.o.f
1A	7.3 ± 0.3	1.95 ± 0.05	5.2 ± 0.2	4.52	1.21/179
1B	11.7 ± 0.8	2.3 ± 0.1	2.7 ± 0.2	2.35	1.13/132
1C	8.4 ± 0.3	1.98 ± 0.05	5.6 ± 0.2	4.82	1.31/199
2A	6.8 ± 0.3	1.97 ± 0.05	1.16 ± 0.06	1.00	1.18/254
2B	5.8 ± 0.2	2.05 ± 0.03	1.09 ± 0.03	0.95	1.36/324
3A	3.9 ± 0.2	1.78 ± 0.04	1.19 ± 0.05	1.03	1.31/206
3B	4.2 ± 0.4	2.04 ± 0.07	1.7 ± 0.1	1.50	1.55/117
3C	3.6 ± 0.2	1.98 ± 0.05	1.04 ± 0.06	0.90	1.25/178
3D	4.3 ± 0.1	2.18 ± 0.04	2.8 ± 0.1	2.38	1.30/254
3E	4.3 ± 0.1	2.28 ± 0.04	3.2 ± 0.1	2.81	1.27/298
3F	5.0 ± 0.2	2.05 ± 0.04	2.6 ± 0.1	2.22	1.40/247
3G	4.5 ± 0.2	1.88 ± 0.04	2.3 ± 0.1	1.98	1.18/199

Table 6. Spectral parameters for each sub-observation obtained using a TBABS∗(POWERLAW + GAUSSIAN) model. Uncertainties quoted are at the 90 per cent confidence level.

Section	N_H [$\times 10^{22}$ cm^{-2}]	Γ	lineE [keV]	EW_{line} [keV]	Unabsorbed Flux [$\times 10^{-11}$ erg cm^{-2} s^{-1}]	Luminosity [$\times 10^{35}$ erg s^{-1}]	χ^2_{red}/d.o.f
1A	12.2 ± 0.5	1.30 ± 0.07	6.36 ± 0.04	0.10 ± 0.06	5.5 ± 0.2	4.74	1.36/172
1B	17 ± 1	1.0 ± 0.1	6.32 ± 0.06	0.13 ± 0.08	2.8 ± 0.2	2.43	1.16/129
1C	15.0 ± 0.3	1.48 ± 0.05	6.38 ± 0.2	0.05 ± 0.04	4.02 ± 0.09	3.47	1.13/242
2A	10.8 ± 0.3	1.28 ± 0.04	6.45 ± 0.05	0.03 ± 0.02	1.12 ± 0.03	0.97	1.21/321
2B	12.7 ± 0.6	1.44 ± 0.07	6.87 ± 0.08	0.07 ± 0.06	1.18 ± 0.06	1.02	1.15/251
3A	8.1 ± 0.4	1.47 ± 0.07	6.5 ± 0.01	0.06 ± 0.04	1.24 ± 0.06	1.07	1.15/204
3B	8.2 ± 0.5	1.19 ± 0.09	6.4 ± 0.3	0.14 ± 0.07	1.8 ± 0.1	1.52	1.53/114
3C	7.4 ± 0.4	1.20 ± 0.07	6.06 ± 0.09	0.05 ± 0.04	1.08 ± 0.06	0.9	1.13/176
3D	8.4 ± 0.3	1.08 ± 0.05	6.43 ± 0.05	0.04 ± 0.03	2.8 ± 0.1	2.43	1.30/252
3E	8.3 ± 0.2	0.98 ± 0.04	6.43 ± 0.04	0.04 ± 0.02	3.3 ± 0.1	2.84	1.25/296
3F	9.6 ± 0.3	1.25 ± 0.05	6.36 ± 0.02	0.10 ± 0.04	2.6 ± 0.1	2.26	1.29/244
3G	8.6 ± 0.4	1.37 ± 0.07	6.39 ± 0.05	0.12 ± 0.06	2.4 ± 0.1	2.06	1.03/196

energy ranges as the previous two observations. At first an absorbed power-law model (CONST∗TBABS∗(POWERLAW)) was used resulting in mainly reasonable fitting parameters. The values for the absorption column density appear to be constant within errors except for section 3F where it is $9.7 \pm 0.3 \times 10^{22}$ cm^{-2} instead of $\sim 8 \times 10^{22}$ cm^{-2}. The photon indices are all around 1.1–1.3 except the one in section 3A, which appears to be slightly higher with a value of 1.47. Similarly, the absorption column densities from the blackbody continuum appear to be constant within errors. We note that 2B and 3A are 2 d apart so given the variability observed, we have no expectation of continuity of parameter values.

Since, when inspecting the individual spectra a hint of a ∼6.4 keV iron-Kα line could be seen, the model was again updated to include this feature. As with the first observation the model (CONST∗TBABS∗(POWERLAW + GAUSSIAN)) resulted in moderately improved fits in those sections where the iron line was found (3B,

Downloaded from https://academic.oup.com/mnras/article/485/1/286/5232390 by CNR user on 14 December 2020

Table 7. Spectral parameters for each sub-observation obtained using a TBABS∗(BLACKBODY + GAUSSIAN) model. Uncertainties quoted are at the 90 per cent confidence level.

Section	N_H [$\times 10^{22}$ cm^{-2}]	kT [keV]	lineE [keV]	EW_{line} [keV]	Unabsorbed Flux [$\times 10^{-11}$ erg cm^{-2} s^{-1}]	Luminosity [$\times 10^{35}$ erg s^{-1}]	χ^2_{red}/d.o.f
1A	7.3 ± 0.3	1.92 ± 0.05	6.4 ± 0.05	0.08 ± 0.04	5.1 ± 0.2	4.45	1.16/179
1B	11.5 ± 0.8	2.3 ± 0.1	6.33 ± 0.06	0.11 ± 0.07	2.6 ± 0.1	2.2	1.08/129
1C	8.4 ± 0.4	1.96 ± 0.05	6.40 ± 0.04	0.05 ± 0.05	5.6 ± 0.2	4.80	1.29/203
2A	5.8 ± 0.2	2.05 ± 0.03	6.4 ± 0.1	0.01 ± 0.01	1.09 ± 0.04	0.95	1.37/321
2B	6.8 ± 0.3	1.97 ± 0.05	6.9 ± 0.3	0.03 ± 0.03	1.16 ± 0.06	1.00	1.20/251
3A	3.9 ± 0.2	1.77 ± 0.04	6.4 ± 0.1	0.04 ± 0.02	1.19 ± 0.06	1.03	1.32/203
3B	4.2 ± 0.4	2.02 ± 0.07	6.4 ± 0.1	0.10 ± 0.06	1.7 ± 0.1	1.49	1.52/114
3C	3.6 ± 0.2	1.98 ± 0.06	6.8 ± 0.5	0.01 ± 0.03	1.7 ± 0.1	0.90	1.27/175
3D	4.2 ± 0.2	2.18 ± 0.04	6.4 ± 0.4	0.01 ± 0.02	2.8 ± 0.1	2.38	1.30/251
3E	4.3 ± 0.1	2.28 ± 0.04	6.4 ± 0.2	0.02 ± 0.20	3.2 ± 0.1	2.80	1.28/295
3F	5.0 ± 0.2	2.03 ± 0.04	6.36 ± 0.07	0.07 ± 0.02	2.6 ± 0.1	2.21	1.35/244
3G	4.5 ± 0.2	1.86 ± 0.04	6.40 ± 0.07	0.07 ± 0.06	2.3 ± 0.1	2.21	1.17/196

3F, and 3G). When trying to fit this model to the other sections, however, the resulting iron line energy was not sensible. Setting the initial value of the parameter around an energy of 6.4 keV did not improve matters. Even so, the other parameters are still consistent with each other in the same way as they were when using an absorbed power-law model without a Gaussian component.

The variation between some of the parameters as well as the χ^2_{red}/d.o.f values are likely due to the rapid fluctuations on short time-scales for this observation. Whilst the Bayesian block analysis suggests to divide the data into seven individual sections some of them still show significant changes in flux occurring at short time-scales, which can affect the quality of the extracted spectrum. A time-resolved spectral analysis with a 1000 s resolution using an absorbed power-law model (Table A1) resulted in χ^2_{red}/d.o.f values between 0.97/72 and 1.47/182. The N_H stayed approximately constant with values $\sim 8 \times 10^{22}$ cm^{-2}; solely towards the end of the observation does it once appear to be higher with a value of 10.2×10^{22} cm^{-2}. The photon index shows small changes with values between 0.89 and 1.57. Overall, the individual spectra do not appear to be too dissimilar such that no different model is needed to interpret the spectral variation which is in agreement with the analysis of the seven sections resulting from the Bayesian block analysis previously. Similarly, the absorbed blackbody model has hydrogen column density values of $\sim 4 \times 10^{22}$ cm^{-2} and temperatures between 1.72 and 2.44 kT.

Much the same as in observation 2 the addition of the Gaussian component to model the iron emission feature is not statistically needed to interpret the different sections of observation 3. The observed X-ray flux varies throughout the observation, however it is never comparable to the flux of the two flares in observation 1 ranging from $\sim$1.1–3.3 $\times 10^{-11}$ erg cm^{-2} s^{-1}. This corresponds to X-ray luminosities between 0.9–2.9 $\times 10^{35}$ erg s^{-1}. All fit parameters for both models are outlined in Tables 4–8.

Fig. 4 plots the spectral parameters obtained for all observations when consistently modelled with an absorbed blackbody continuum. It is evident that the contours overlap within each observation. One of the contours in observation 2 overlaps with one from observation 1 whilst the other one from observation 2 overlaps with one from observation 3. Consequently, a decrease in hydrogen column density can be observed throughout the observations. The only contour that is not connected to any other is the one from section 1B where the hydrogen column density is about twice as high as the average value obtained from the other sections.

Fit results for an absorbed power-law model and an absorbed blackbody model have been discussed in detail, and have been used primarily as consistent reference models when subdividing the data set in a search for spectral variations. More complex, science-driven models often used in fitting SFXT spectra were also investigated, but in most cases failed due to a lack of statistics when considering short sections of data. For example, a Comptonizing plasma model CONST∗TBABS∗(COMPTT) and a cut-off power-law CONST∗TBABS∗(CUTOFFPL) failed to give better fits to the data and often resulted in unphysical or unconstrained parameters. Fitting a Comptonizing plasma model to section 1A results in χ^2_{red}/d.o.f = 1.43/173 with kT = 215 ± 2944 keV, a seed photon temperature of $T_0 = 0.3 \pm 1.0$ keV, and an optical depth of $\tau = 0.8 \pm 102.0$. As another example, a cut-off power law fitted to section 3A gave an $N_H = 6.5 \pm 0.7 \times 10^{22}$ cm^{-2}, a photon index of $\Gamma = 0.5 \pm 0.4$ and a high energy cut-off of 6 ± 2 keV. These problems are likely due to the lack of significant data above 10 keV required to constrain the additional fit components.

By performing time-resolved spectral analysis (using a simple power-law model) we investigated if there is a correlation between the hardness and flux of the source in observations 2 and 3. The Pearson correlation coefficient (where a value of zero means there is no correlation, −1 is an exact negative, + 1 is an exact positive linear correlation) was calculated to measure the linear relationship between hardness and flux. Combining the results of observations 2 and 3 resulted in a correlation coefficient of −0.27, implying that the flux values and photon indices are not correlated (Fig. 5). The same analysis was unsuccessful for observation 1 due to the higher error values, resulting from the pile-up reduction, making it impossible to create the individual spectra needed for the time-resolved spectral analysis.

3.5 Temporal analysis

Less than half of the confirmed SFXTs have a known spin period for their suspected neutron star accretor. Those identified range from a possible ∼5 s in AX J1841.0−0536 (Bamba et al. 2001) to ∼1212 s in IGR J16418−4532 (Sidoli et al. 2012). Previous observations of IGR J17354−3255 have failed to find a periodic signal that can be interpreted as the spin period of the neutron star (Ducci et al. 2013).

We searched for periodicities in the range 0.1–500 s using both unbinned and binned (where appropriate) methods. The primary

Downloaded from https://academic.oup.com/mnras/article/485/1/286/5232390 by CNR user on 14 December 2020

Table 8. Time-resolved spectral analysis of observation 3 with a resolution of 1000 s using the TBABS∗BLACKBODY model. Uncertainties quoted are at the 90 per cent confidence level.

Number	χ^2_{red}	dof	N_H [$\times 10^{22}$ cm^{-2}]	kT [keV]	Flux [$\times 10^{-11}$ erg cm^{-2} s^{-1}]
1	1.12	68	4.0 ± 1.1	1.7 ± 0.2	0.74 ± 0.05
2	1.11	180	3.5 ± 0.5	1.7 ± 0.1	1.29 ± 0.06
3	1.04	214	3.8 ± 0.4	1.7 ± 0.1	1.63 ± 0.06
4	1.00	168	4.4 ± 0.7	1.8 ± 0.1	1.09 ± 0.05
5	1.49	178	4.8 ± 0.6	1.9 ± 0.1	1.23 ± 0.05
6	1.39	185	4.3 ± 0.5	1.9 ± 0.1	1.28 ± 0.04
7	1.19	122	3.6 ± 0.7	1.8 ± 0.1	0.69 ± 0.04
8	1.08	134	3.4 ± 0.7	1.9 ± 0.1	0.79 ± 0.04
9	1.08	106	3.5 ± 0.8	2.0 ± 0.2	0.65 ± 0.04
10	0.99	166	3.7 ± 0.6	2.1 ± 0.1	1.15 ± 0.05
11	1.04	218	3.9 ± 0.4	2.0 ± 0.1	1.74 ± 0.05
12	1.04	237	4.2 ± 0.4	1.9 ± 0.1	2.27 ± 0.07
13	1.03	251	4.3 ± 0.4	2.1 ± 0.1	2.69 ± 0.08
14	1.13	269	4.9 ± 0.4	2.4 ± 0.1	3.44 ± 0.08
15	1.26	299	4.6 ± 0.3	2.4 ± 0.1	4.23 ± 0.09
16	1.16	281	4.7 ± 0.4	2.2 ± 0.1	3.63 ± 0.08
17	1.17	249	5.1 ± 0.5	2.1 ± 0.1	2.66 ± 0.08
18	1.05	213	5.0 ± 0.5	2.1 ± 0.1	1.80 ± 0.06
19	0.98	191	5.3 ± 0.6	2.0 ± 0.1	1.49 ± 0.05
20	1.08	237	4.8 ± 0.4	1.8 ± 0.1	1.99 ± 0.07

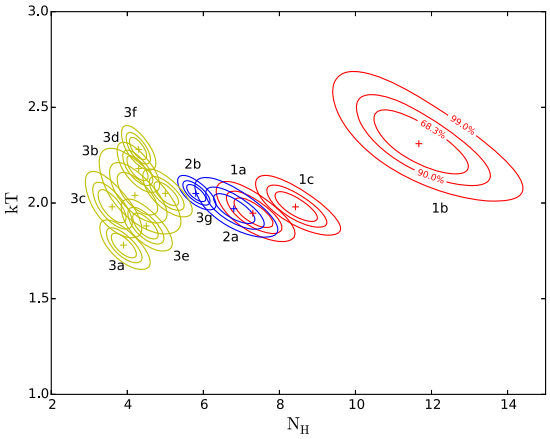

Figure 4. Contour plots for the spectral parameters measured from all observations (Observation 1 is red, observation 2 is blue, and observation 3 is yellow). The contours correspond to the 68 per cent, 90 per cent, and 99 per cent confidence levels.

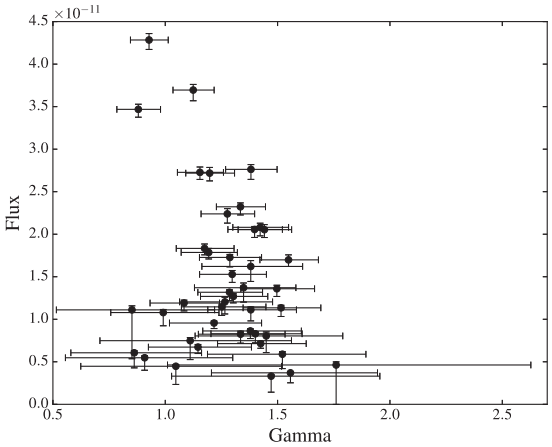

Figure 5. Time-resolved analysis of flux and photon index through observations 2 and 3. Each data point is derived from a 1000 s subsection of data.

method used was a Z_n^2 method (Buccheri et al. 1983) applied to event lists created from the source locations in the cleaned observation event lists. The upper period range for which our search was set by the time-scales of the flaring structures (∼1000 s) in the light curves, which inject red noise into the analysis. These tests were supported by randomization Monte Carlo tests to determine the noise levels within the periodiograms, but we must consider that such tests are only sensitive to white noise, and provide only an lower limit to the confidence levels for powers seen in the periodograms.

We found no evidence for a persistent periodicity in the light curves for observations 1 and 2, the periodogram powers seen up to ∼500 s is consistent with white noise, and beyond 500 s the periodicity analysis is strongly impacted by the non-periodic structures easily seen in the light curves on 1000 s time-scales. There was tentative evidence for a 251 s period in the three light curves of observation 3, but in this case the source PSF is badly affected by a CCD feature which cannot be corrected for in an event-based analysis.

Binned light curves were extracted for all cameras in observation 1 (10 s binning) and observations 2 and 3 (1 s binning); the bin sizes were chosen as a compromise between avoiding empty bins considering the mean count rates of the source, and retaining sensitivity to short-period signals. As a result of this necessary compromise, binned methods are less optimal for low statistics light curves such as these. A Lomb–Scargle periodogram (Lomb 1976; Scargle 1982) was produced using the fast implementation of Press & Rybicki (1989) for each binned light curve. These tests were again supported by randomization Monte Carlo tests to determine the noise levels within the periodiograms. No significant (> 99 per cent) probability periodicities were detected in the range 2xbinsize – 500 s. An epoch folding method using the Q^2 statistic as defined by Leahy et al. (1983) was used to further test the binned

Downloaded from https://academic.oup.com/mnras/article/485/1/286/5232390 by CNR user on 14 December 2020

light curves for period signals. Again, no significant peaks were identified. The binned analysis was unable to replicate or confirm the tentative 251 s period seen in the unbinned analysis.

4 DISCUSSION

We present the results of three *XMM–Newton* observations of the SFXT, IGR J17354−3255. Observation 1 was performed at a phase range $\phi = 0.154$–0.199, as an initial trial pointing, resulting in the source only being observed by the two EPIC-MOS cameras. Observations 2 and 3 were carried out approximately two weeks later closer to system periastron (at phase ranges $\phi = 0.804$–0.839 and $\phi = 0.996$–0.025, respectively) and with the instruments in a more appropriate configuration. Significant flux variations and flaring were detected in all three observations. In order to avoid averaging spectral analysis across different source behaviours, a Bayesian block method was utilized in order to objectively characterize possible changes in spectral hardness through the three observations. As a result, the three observations were split into 12 separate subsections for which individual spectra were extracted.

4.1 Continuum emission and absorption column

A spectral analysis of all the sections revealed that the source continuum X-ray emission could be described just as well by either a Tuebinger–Boulder ISM absorption model with a power law or a blackbody.

The photon index derived from the power-law fits varied over the range $\Gamma = \sim 1.0$–1.5, with a typical error of $\sim \pm 0.1$, suggesting significant changes. However, there is no obvious trend or evolution indicating that these changes in photon index are correlated with other parameters (see later).

The absorption column density varied significantly across the three sections of observation 1, reaching $N_H \sim 17 \times 10^{22}$ cm^{-2} at its highest. This corresponded in time to a period of low flux between flaring. The power-law fits for observation 2 and observation 3 showed slowly declining N_H values of typically $N_H \sim 11 \times 10^{22}$ cm^{-2} and $N_H \sim 8 \times 10^{22}$ cm^{-2}, respectively. The same trend was seen in the blackbody model fits, where the absorption column density increased to a maximum of $N_H = 11.7 \times 10^{22}$ cm^{-2} in section 1B and then declined back down to $N_H \sim 4 \times 10^{22}$ cm^{-2} through observations 2 and 3.

Our measurements of column density are in broad agreement with previous observations of IGR J17354−3255 (Tomsick 2009; D'Aì et al. 2011) suggesting that the average absorption column density of this source in quiescence is ~ 4–8×10^{22} cm^{-2}. The expected absorption in the direction of the source is considerably less ($N_H = 1.50 \times 10^{22}$ cm^{-2} (Dickey & Lockman 1990) suggesting that a fraction of the absorbing medium is intrinsic to the binary system. While previous observations of the source have already revealed a high absorbing column density of $(7.5$–$10) \times 10^{22}$ cm^{-2} (Tomsick 2009, D'Aì et al. 2011), the absorption detected between the flares in observation 1 is still about a factor of two higher than any previously measured in this source. Absorbing column densities of this level have previously been seen in other SFXTs such as IGR J18410−0535 (Bozzo et al. 2011) and SAX J1818.6−1703 (Boon et al. 2016). The former measured an increase in N_H from 3–20×10^{22} cm^{-2} with a further increase to a value of $\sim 50 \times 10^{22}$ cm^{-2} towards the end of the observation. Their analysis provided evidence that the flare was produced due to the ingestion of a clump of matter. The single incidence of a high absorption column density between two flares seen in observation 1 is most likely caused by changes in the local environment around the compact object rather than any change in the underlying continuum emission mechanism.

The spectral parameters measured during observations 2 and 3 show minimal variation with intrinsic absorption column density values between $N_H = 8$–12×10^{22} cm^{-2} with the power-law model and $N_H = 4$–7×10^{22} cm^{-2} with the blackbody model. Photon index values lie between $\Gamma = \sim 1.0$–1.5 and blackbody temperatures are typically of ~ 2 keV. Whilst the blackbody temperatures seem high on first inspection they are consistent with those associated with the surface of an accreting neutron star (Bartlett, Coe & Ho 2013; Lotti et al. 2016). The same XSPEC model used in observation 1 could be utilized to describe the X-ray emission from IGR J17354−3255 during all observations, and hence the spectral evolution is most simply explained by a relatively constant underlying continuum shape with changes occurring due to varying absorption.

Observation 3 exhibits considerable fast flaring, and whilst the absorption column density is near constant, the rapidly varying photon index is likely due to averaging spectra across the rapid changes in flux. A time-resolved spectral analysis was utilized to look into this phenomenon in more detail. The absorption column density was mostly constant around $\sim 8 \times 10^{22}$ cm^{-2} but even at higher timing resolution, the photon index still varied between 0.9 and 1.6. Whilst the difference is not great it could indicate changes to the underlying emission mechanism or (more likely considering the time-scales involved) could also be explained by the local changes in N_H. Due to the statistical properties of the spectra, however, we are unable to investigate more complex models to explain the behaviour in observation 3.

4.2 Correlated flux – spectral changes?

While the power-law index was seen to vary significantly through the observations, we were unable to establish any correlations of these changes in photon index with other fit parameters, or with the source brightness. In particular, the association of a hard spectrum and low flux seen in observation 1B was not seen to hold across the remainder of the data set, and must be considered a one-off event based on the current data set.

In a wider context of SFXT behaviour, observation section 1B may be an example of 'pre-flare hardening' – a sudden increase in the absorption column density together with a decrease in flux associated with subsequent flares. This feature may be seen due to a dense clump of material travelling towards the neutron star during this time. Whilst the N_H had a significant rise in section 1B, the photon index only showed minimal variability. This phenomenon could be a sign of absorption of a constant intrinsic flux by an optically thin material. Similar behaviour has been observed in SFXTs like IGR J18410−0535 (Bozzo et al. 2011) and IGR J16418−4532 (Drave et al. 2013), where the resulting conclusion was that an optically thin clump of stellar wind material obscured the intrinsic emission from the neutron star. The clumpy wind model is often used to interpret the X-ray variability of SFXTs (in 't Zand 2005; Walter & Zurita Heras 2007; Ducci et al. 2009). The model predicts that fast X-ray flaring can be produced when the neutron star sporadically captures and accretes a clump of stellar wind material. Clumps that pass in front of the X-ray source may cause temporary dimming or obscuration. Therefore we conclude that the absorption features present in observation 1 may represent structures in the wind i.e. a clump being accreted causing a flare in section 1A, a further optically thin clump of stellar wind material obscuring the

Downloaded from https://academic.oup.com/mnras/article/485/1/286/5232390 by CNR user on 14 December 2020

intrinsic emission from the neutron star in section 1B and then the latter being captured and accreted in section 1C.

A time-resolved spectral analysis performed at 1000 s resolution on observation 3 using a simple power-law model did not show any significant correlation between the continuum flux and photon index. This result agrees with the findings of Bozzo et al. (2017) whose analysis of the HR versus the flux shows no significant variation. There is therefore no evidence that IGR J17354−3255 follows the 'harder-when-brighter' correlation seen in some other sources.

4.3 The broad-band spectrum

Extrapolating the mean *XMM–Newton* flux to an 18–60 keV flux enabled direct comparison with the upper flux limits obtained with the *INTEGRAL* analysis. An average flux of 2.6×10^{-11} erg cm^{-2} s^{-1} in the 1–12 keV band is equivalent 6.65×10^{-11} erg cm^{-2} s^{-1} in the 18–60 keV band (IBIS/ISGRI) and 1.80×10^{-11} erg cm^{-2} s^{-1} in the 3–10 keV band (JEM-X). The JEM-X upper limit on the persistent flux was found to be 1.35×10^{-11} erg cm^{-2} s^{-1}, similar to the extrapolated flux. Conversely, the extrapolated 18–60 keV flux is far in excess of the IBIS/ISGRI upper limit on the persistent flux of 1.00×10^{-11} erg cm^{-2} s^{-1}, providing strong evidence that the simple power-law spectrum does not extend above 10 keV and consequently a cut-off power-law would be needed to explain the IBIS/ISGRI upper limit. It was not possible to constrain a cut-off power-law model using the *XMM–Newton* spectra alone, suggesting that the cut-off likely appears somewhere between 10–30 keV. The average *XMM–Newton* flux for the blackbody model resulted in an 18–60 keV flux of 1.3×10^{-12} erg cm^{-2} s^{-1}, which is consistent with the IBIS/ISGRI upper limit. Consequently, a single power law can be ruled out as the optimal model to fit to the available *XMM–Newton* data.

The non-detection of outburst activity by *INTEGRAL* is consistent with the particularly low outburst recurrence of this source. Sguera et al. (2011) states that the recurrence rate for emission detectable by *INTEGRAL* at periastron is only ∼25 per cent.

4.4 Presence of an iron line?

In some spectra, residuals in the fit around 6.5 keV hinted at a line feature. Any underlying iron line is likely caused by X-ray irradiation of cold iron in the wind of the supergiant (Kallman et al. 2004). Adding a Gaussian component to account for an iron emission feature improved the fits marginally (but within the errors on the fit statistic) in many cases, and somewhat reduced the residuals in the fit (Fig. 6). In most cases, we were able to obtain constrained errors on the equivalent widths using the XSPEC EQWIDTH tool. In these instances, the line is (as expected from inspection) of marginal significance at best. We note here that the F-test statistic is not suitable to test for the presence of a line, and we can only estimate the significance of the line detection from the errors on the equivalent width, when it is constrained.

4.5 Comparison with previous analysis

The results of our work generally agree with the findings of Bozzo et al. (2017). They fit an absorbed power-law model and achieved reasonable results. However, when also considering the *INTEGRAL* upper limit, a blackbody model may be a better fit. Moreover, they found that the addition of an iron line further improved the fits, but

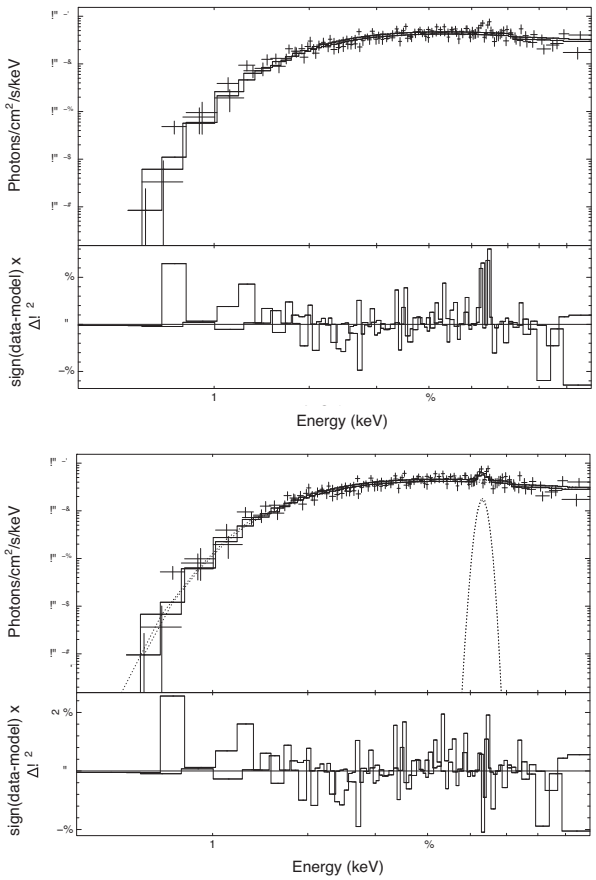

Figure 6. Top panel: Blackbody fit with residuals to EPIC-MOS1 and EPIC-MOS2 spectra from observation 1B. Bottom panel: Blackbody fit with an additional Gaussian component from the same observation.

we are unable to confirm that in detail due to the statistical quality of the time-resolved spectra we used.

The interpretation that the decrease in flux together with an increase in the absorption column density between the two flares in observation 1 could be due to a clump of matter obscuring the source further agrees with their results. It is generally considered that simple ingestion of clumps of matter cannot be the sole reason for the high X-ray variability in SFXTs and there must be mechanisms present that inhibit the accretion of the stellar wind material, Bozzo et al. (2017) concluded that IGR J17354−3255 seems to have no issues overcoming them. We also see no evidence of spectral changes beyond variable absorption and accretion rate.

ACKNOWLEDGEMENTS

We would like to thank Diego Altamirano, Angela Bazzano, and Lara Sidoli for their helpful discussions on the analysis techniques used. This work is based on data from observations with *XMM–Newton* . *XMM–Newton*is an European Space Agency (ESA) science mission with instruments and contributions directly funded by ESA Member States and the USA (NASA). MEG is supported by a Mayflower Scholarship from the University of Southampton. ABH acknowledges that this research was supported by a Marie Curie International Outgoing Fellowship within the 7th European Community Framework Programme (FP7/2007 − 2013) under grant no. 275861. SPD acknowledges support from the UK Science

Downloaded from https://academic.oup.com/mnras/article/485/1/286/5232390 by CNR user on 14 December 2020

And Technology Facilities Council, STFC. This research has made use of the SIMBAD data base, operated at CDS, Strasbourg, France. This research made use of APLPY, an open-source plotting package for PYTHON (Robitaille & Bressert 2012).

REFERENCES

Bamba A., Yokogawa J., Ueno M., Koyama K., Yamauchi S., 2001, PASJ, 53, 1179
Barthelmy S. D. et al., 2005, Space Sci. Rev., 120, 143
Bartlett E. S., Coe M. J., Ho W. C. G., 2013, MNRAS, 436, 2054
Baumgartner W. H., Tueller J., Markwardt C., Skinner G., 2010, BAAS, 41, 675
Bird A. J. et al., 2016, ApJS, 223, 15
Boon C. M. et al., 2016, MNRAS, 456, 4111
Bozzo E., Falanga M., Stella L., 2008, in proceedings of "7th INTEGRAL Workshop", Sep., PoS(INTEGRAL2008). Proceedings of Science/SISSA, Trieste, Italy, p. 101
Bozzo E. et al., 2011, A&A, 531, A130
Bozzo E., Pavan L., Ferrigno C., Falanga M., Campana S., Paltani S., Stella L., Walter R., 2012, A&A, 544, A118
Bozzo E., Bernardini F., Ferrigno C., Falanga M., Romano P., Oskinova L., 2017, A&A, 608, A128
Buccheri R. et al., 1983, A&A, 128, 245
Bulgarelli A. et al., 2009, Astron.Telegram , 2017
Clark D. J. et al., 2010, MNRAS, 406, L75
Coleiro A., Chaty S., Heras J. A. Z., Rahoui F., Tomsick J. A., 2013, A&A, 560, A108
Cusumano G. et al., 2010, A&A, 524, A64
D'Aì A., La Parola V., Cusumano G., Segreto A., Romano P., Vercellone S., Robba N. R., 2011, A&A, 529, A30
den Herder J. W. et al., 2001, A&A, 365, L7
Dickey J. M., Lockman F. J., 1990, ARA&A, 28, 215
Drave S. P., Bird A. J., Sidoli L., Sguera V., McBride V. A., Hill A. B., Bazzano A., Goossens M. E., 2013, MNRAS, 433, 528
Ducci L., Sidoli L., Mereghetti S., Paizis A., Romano P., 2009, MNRAS, 398, 2152
Ducci L., Romano P., Esposito P., Bozzo E., Krimm H. A., Vercellone S., Mangano V., Kennea J. A., 2013, A&A, 556, A72
Gabriel C. et al. , 2004, in Ochsenbein F., Allen M. G., Egret D., eds, ASP Conf. Ser., Vol. 314, Astronomical Data Analysis Software and Systems (ADASS) XIII. Astron. Soc. Pac., San Francisco, p. 759
Hill A., 2016, bayesBlocks: First alpha release, Zenodo
in't Zand J. J. M., 2005, A&A, 441, L1
Jethwa P., Saxton R., Guainazzi M., Rodriguez-Pascual P., Stuhlinger M., 2015, A&A, 581, A104
Kallman T. R., Palmeri P., Bautista M. A., Mendoza C., Krolik J. H., 2004, ApJS, 155, 675
Kuulkers E. et al., 2006, Astron. Telegram, 874
Kuulkers E., et al., 2007, A&A, 466, 595
Leahy D. A., Darbro W., Elsner R. F., Weisskopf M. C., Sutherland P. G., Kahn S., Grindlay J. E., 1983, ApJ, 266, 160
Lomb N. R., 1976, Ap&SS, 39, 447
Lotti S. et al., 2016, ApJ, 822, 57
Lund N. et al., 2003, A&A, 411, L231
Negueruela I., Smith D. M., Reig P., Chaty S., Torrejon J. M., 2006, in Wilson A., ed., ESA SP-604: Supergiant Fast X-ray Transients: A New Class of High Mass X-ray Binaries Unveiled by INTEGRAL. ESA, Noordwijk, p. 165
Press W. H., Rybicki G. B., 1989, ApJ, 338, 277
Read A. M., Guainazzi M., Sembay S., 2014, A&A, 564, A75
Robitaille T., Bressert E., 2012, Astrophysics Source Code Library, record ascl:1208.017
Romano P. et al., 2015, A&A, 576, L4
Scargle J. D., 1982, ApJ, 263, 835
Scargle J. D., Norris J. P., Jackson B., Chiang J., 2013, ApJ, 764, 167
Sguera V. et al., 2005, A&A, 444, 221
Sguera V. et al., 2006, ApJ, 646, 452
Sguera V. et al., 2007, A&A, 462, 695
Sguera V., 2013, Nucl. Phys., 239, 76
Sguera V., Drave S. P., Bird A. J., Bazzano A., Landi R., Ubertini P., 2011, MNRAS, 417, 573
Shakura N., Postnov K., Sidoli L., Paizis A., 2014, MNRAS, 442, 2325
Sidoli L., Mereghetti S., Sguera V., Pizzolato F., 2012, MNRAS, 420, 554
Strüder L. et al., 2001, A&A, 365, L18
Tomsick J. A., 2009, Astron. Telegram, 2022
Tomsick J. A., Chaty S., Rodriguez J., Walter R., Kaaret P., 2009, ApJ, 701, 811
Turner M. J. L. et al., 2001, A&A, 365, L27
Ubertini P. et al., 2003, A&A, 411, L131
Vedrenne G. et al., 2003, A&A, 411, L63
Walter R., Zurita Heras J., 2007, A&A, 476, 335
Wilms J., Allen A., McCray R., 2000, ApJ, 542, 914

APPENDIX A: ADDITIONAL TIME-RESOLVED SPECTRAL ANALYSIS USING A TBABS∗POWERLAW MODEL

Downloaded from https://academic.oup.com/mnras/article/485/1/286/5232390 by CNR user on 14 December 2020

Table A1. Time-resolved spectral analysis with a resolution of 1000 s of observation 3 using the tbabs∗powerlaw model. The model parameters as well as their lower and upper limits are displayed.

Number	χ^2_{red}	dof	N_H [$\times 10^{22}$ cm^{-2}]	N_HLL [$\times 10^{22}$ cm^{-2}]	N_HUL [$\times 10^{22}$ cm^{-2}]	Gamma	GammaLL	GammaUL	Flux [erg cm^{-2} s^{-1}]	FluxLL [erg cm^{-2} s^{-1}]	FluxUL [erg cm^{-2} s^{-1}]
1	0.97	72	8.18	6.76	9.81	1.44	1.16	1.75	8.05E-12	6.51E-12	8.43E-12
2	1.07	184	7.53	6.73	8.41	1.47	1.32	1.63	1.37E-11	1.28E-11	1.40E-11
3	1.06	218	8.13	7.43	8.90	1.54	1.42	1.67	1.70E-11	1.63E-11	1.74E-11
4	1.00	172	9.46	8.49	10.54	1.57	1.41	1.74	1.12E-11	1.05E-11	1.16E-11
5	1.47	182	8.73	7.88	9.68	1.28	1.14	1.43	1.28E-11	1.21E-11	1.31E-11
6	1.38	189	8.26	7.43	9.17	1.26	1.12	1.40	1.33E-11	1.26E-11	1.36E-11
7	1.13	126	7.81	6.81	8.93	1.40	1.22	1.60	7.18E-12	6.56E-12	7.45E-12
8	0.99	138	7.59	6.65	8.65	1.34	1.16	1.52	8.25E-12	7.62E-12	8.52E-12
9	1.06	110	7.64	6.38	9.13	1.17	0.97	1.39	6.68E-12	6.10E-12	6.97E-12
10	0.97	170	7.72	6.85	8.68	1.15	1.01	1.30	1.17E-11	1.10E-11	1.21E-11
11	1.02	222	8.01	7.30	8.78	1.22	1.10	1.34	1.78E-11	1.70E-11	1.82E-11
12	1.05	241	8.52	7.87	9.23	1.33	1.22	1.44	2.33E-11	2.24E-11	2.38E-11
13	1.13	255	8.47	7.80	9.19	1.15	1.05	1.25	2.73E-11	2.64E-11	2.79E-11
14	1.17	274	9.12	8.41	9.88	0.89	0.79	0.98	3.46E-11	3.35E-11	3.53E-11
15	1.21	304	8.56	8.00	9.17	0.93	0.85	1.01	4.28E-11	4.17E-11	4.37E-11
16	1.13	286	9.07	8.47	9.72	1.12	1.03	1.21	3.70E-11	3.60E-11	3.77E-11
17	1.18	253	9.73	8.98	10.54	1.20	1.09	1.31	2.72E-11	2.62E-11	2.78E-11
18	1.06	217	9.34	8.48	10.29	1.17	1.05	1.30	1.83E-11	1.77E-11	1.87E-11
19	1.02	195	10.20	9.18	11.34	1.30	1.16	1.44	1.53E-11	1.44E-11	1.57E-11
20	1.07	241	9.38	8.65	10.17	1.43	1.32	1.55	2.06E-11	1.97E-11	2.10E-11
21	1.03	243	8.24	7.63	8.90	1.40	1.29	1.51	2.75E-11	2.64E-11	2.82E-11

This paper has been typeset from a TEX/LATEX file prepared by the author.

Downloaded from https://academic.oup.com/mnras/article/485/1/286/5232390 by CNR user on 14 December 2020